Nano Research 2015, 8(11): 3553–3561
DOI 10.1007/s12274-015-0855-2
Research Article
ISSN 1998-0124
CN 11-5974/O4

A facile synthesis of hierarchical Sn_3O_4 nanostructures in an acidic aqueous solution and their strong visible-light-driven photocatalytic activity

Hui Song[1], Su-Young Son[1,2], Seul Ki Kim[1], and Gun Young Jung[1] (✉)

[1] *School of Materials Science and Engineering, Gwangju Institute of Science and Technology (GIST), Gwangju 500-712, Republic of Korea*
[2] *Carbon Convergence Materials Research Center, Institute of Advanced Composite Materials, Korea Institute of Science and Technology (KIST), Jeollabuk-do 565-905, Republic of Korea*

Received: 11 May 2015
Revised: 21 June 2015
Accepted: 6 July 2015

KEYWORDS
Sn_3O_4,
hierarchical structure,
hydrothermal,
morphology engineering,
photocatalyst

ABSTRACT

Hierarchical tin(III) oxide, Sn_3O_4, nanospheres were synthesized via hydrothermal reaction under strongly acidic ambient conditions. The morphology of Sn_3O_4 varied with decreasing pH. The prickly Sn_3O_4 nanospheres changed into Sn_3O_4 nanospheres covered with single-crystalline nanoplates having a high BET surface area of ca. 55.05 $m^2 \cdot g^{-1}$ and a band gap of ca. 2.25 eV. Small amounts (0.05 g) of the hierarchical Sn_3O_4 nanostructures completely decomposed a 30% methyl orange (MO) solution in 100 mL deionized water within 15 min under one sun condition (UV + visible light). The Sn_3O_4 photocatalyst exhibited a fast decomposition rate of 1.73×10^{-1} min^{-1}, which is a 90.86% enhancement relative to that of the commercially available P25 photocatalyst. The high photocatalytic activity of the hierarchical Sn_3O_4 nanostructures is attributed to its ability to absorb visible light and its high surface-to-volume ratio.

1 Introduction

Tin oxide has several advantages, such as controllable size or shape when synthesized via the simple hydrothermal method [1], excellent optical and electrical properties (transparency at wavelengths of 300–800 nm and a low electronic resistivity of 8.6×10^{-5} $\Omega \cdot \square^{-1}$), and its non-toxicity [2]. With these merits, it has been utilized in various fields such as gas sensors [3, 4], lithium ion batteries [5], dye-sensitized solar cells [6], and photocatalysts [7–9]. Regarding its use as a photocatalyst, tin oxide has strong resistance against acidic/alkaline solutions and exhibits good photocatalytic activity without generating secondary pollutants under irradiation with ultraviolet (UV) light [8, 9]. However, because of its wide band gap, there are few works reporting the use of tin oxides alone under visible light irradiation. Therefore, co-catalysts with narrow energy band gaps, such as CdS [10], $Ru(bpy)_3^{2+}$ [11], and Pt [12], have been introduced to enhance the photocatalytic activity of tin oxide under visible light irradiation. However, the high cost of co-catalysts

Address correspondence to gyjung@gist.ac.kr

necessitates the development of photo-catalytic materials that can generate electron-hole pairs under visible light and thus effectively use sunlight.

Unlike SnO_2, Sn_3O_4 has been experimentally shown to absorb light at visible wavelengths [13–15] and thus has been used as a visible-light-driven photocatalyst. The pollution decomposition efficiency of Sn_3O_4 photocatalyst under sunlight is higher than that of SnO_2 [13]. However, studies on Sn_3O_4 have begun only recently, including investigations into its growth mechanism [16–18], crystal structure, and theoretical properties [19, 20].

Sn_3O_4 is one of the three intermediates (i.e., Sn_3O_4, Sn_2O_3 and Sn_5O_6) formed during the disproportionation reaction of Tin(II) oxide (SnO) [21]. Sn_3O_4 is mainly generated by dry chemical methods including carbothermal evaporation [15], thermal decomposition of SnO [22], and carbothermal reduction [23]. Vilasi et al. reported that Sn_3O_4 coexists as a transition form at the process temperature range of 400–500 ℃ during the phase transformation from SnO to SnO_2 [24]. However, only a small quantity of Sn_3O_4 was obtained by this method. Instead, SnO_2 was obtained as the major product during the oxidation of Sn^{2+} at high temperatures, as it is thermodynamically more stable than Sn_3O_4.

For this reason, hydrothermal methods were used to produce Sn_3O_4 below 200 ℃ without the production of unwanted SnO_2 [25–29]. Li et al. hydrothermally synthesized hierarchical Sn_3O_4 structures (diameter: ~1 μm) at 180 ℃ and pH 3 in a Teflon autoclave vessel, which made it difficult to adjust the pH for controlling the morphology. They showed that the hierarchical Sn_3O_4 structure had the highest pollution decomposition rate among photocatalysts such as SnO, SnO_2, and N-doped TiO_2 [13]. However, in 20 min, only 10 ppm of methyl orange (MO) in an 80 mL solution was decomposed by the photocatalytic reaction of 0.04 g Sn_3O_4.

Here we propose a facile hydrothermal method for fabricating hierarchical Sn_3O_4 nanospheres covered with single-crystalline nanoplates below 100 ℃ using a three-necked round-bottom flask. By adjusting the pH of the nutrient solution during the process, the morphology and phase transformation of SnO into the Sn_3O_4 nanostructures can be controlled. The photocatalytic activity of the generated hierarchical Sn_3O_4 nanostructures was investigated and compared with that of the commercially available TiO_2 (Degussa, P25) under one sun condition (i.e., Air Mass 1.5, 100 mW·cm^{-2}).

2 Experimental section

2.1 Synthesis of hierarchical Sn_3O_4 nanostructures

At room temperature, 1.23 g of tin oxalate ($Sn(C_2O_4)$, M = 206.78 g·mol^{-1}) was dissolved in 250 mL deionized (DI) water with stirring for 30 min. When the temperature reached 70 ℃, black precipitate of SnO appeared. Then, the pH of the nutrient solution was adjusted (pH = 2, 3, 4, and 5) by slowly adding 0.5 M hydrochloric acid (HCl, M = 40.06 g·mol^{-1}, 37%) to the solution containing the black precipitate, while continuously stirring for 3 h at 95 ℃. The color of the precipitate changed from black to yellow. After completion of the hydrothermal reaction, the precipitate was collected by centrifugation and then washed with DI water. Finally, the product was dried inside a common laboratory oven at 35 ℃ for 1 day.

2.2 Characterization of properties

The crystallographic information of the hierarchical Sn_3O_4 nanostructures was obtained by X-ray diffraction (XRD) using Cu K-alpha radiation (40 kV, 100 mA, Rigaku D/max-2400) and by Raman spectroscopy with a 514 nm laser (Horiba). The morphology of the sample was observed by scanning electron microscopy (SEM, FE-SEM, JEOL 2010 F) and high-resolution transmission electron microscopy (HRTEM, JEM-2100), operated at an accelerating voltage of 200 kV. The specific surface area was measured by the Brunauer-Emmett-Teller (BET) method using a nanoporosity surface area analyzer (nanoPOROSITY-XQ, Mirae Scientific Instruments Inc.). A UV-visible spectrometer (AvaSpec-ULS2048L-USB2 Spectrometer, Jinyoung tech Inc.) was used to analyze the absorbance of the hierarchical Sn_3O_4 nanostructures and the decomposition of the MO solution. Photocatalytic activity was characterized under illumination with an AM 1.5 simulated sunlight source (SANEI solar simulator, one sun condition, Class A) with a power density of 100 ± 2.5 mW·cm^{-2}.

2.3 Photocatalytic activity

0.05 g of the as-produced SnO and Sn_3O_4 catalysts, and the commercially available P25 (TiO_2, Degusa) were added to a 30 vol.% MO solution in 100 mL DI water. Prior to irradiation, the suspension was violently stirred in the dark for 30 min to saturate the solution with O_2. The suspension was irradiated with light (UV + visible) from a solar simulator. At specific time intervals (15, 30, 45, and 60 min), a 3 mL aliquot was extracted and filtered to remove the photocatalytic powder. The filtered solution was analyzed by the UV-visible spectrometer to measure the MO contents (maximum absorption band λ = 485 nm).

3 Results and discussion

3.1 Effect of pH on the formation of the hierarchical Sn_3O_4 nanostructures

The hierarchical Sn_3O_4 nanostructures were synthesized by hydrothermal reaction at 95 ℃. Tin oxalate, $Sn(C_2O_4)$, was used as the source of tin ions. Unlike most commonly used tin salts such as tin dichloride ($SnCl_2$) and tin tetrachloride ($SnCl_4$), $Sn(C_2O_4)$ easily dissociates at low temperatures producing a large number of Sn^{2+} ions in the nutrient solution. This is because of the relatively weak electrostatic attraction between the pure metal ion (Sn^{2+}) and the organic chelating agent ($[C_2O_4]^{2-}$) [6]. Thus, first, SnO was easily synthesized using $Sn(C_2O_4)$ as a starting material at low temperature. Then, under acidic conditions, SnO easily dissolves to form a tin complex ion ($[Sn_3(OH)_4]^{2+}$). Finally, the Sn_3O_4 nanostructures were formed by dehydration of $[Sn_3(OH)_4]^{2+}$ [30].

When the temperature of the nutrient solution reached 70 ℃, the color of the precipitate changed from white to black, indicating the formation of SnO, and remained black until 95 ℃. However, on adding hydrochloric acid solution at 95 ℃, the color of the precipitate changed to yellow, suggesting that some changes occurred in the SnO.

The morphology and phase transformation of the products were examined at different pH values, which was controlled by varying the amount of hydrochloric acid added to the solution. After completion of the hydrothermal reaction, the precipitate was collected by centrifugation and then dried to analyze its structure and determine its photocatalytic activity.

The crystallographic structures of the hierarchical Sn_3O_4 nanostructures at various pHs were characterized by XRD, as shown in Fig. 1. Figure 1(a) indicates the XRD peaks of a tetragonal SnO, marked with the ● symbol at (001), (101), and (002), which match well with the standard XRD data file (JCPDS-06-0395). The phase transformation from SnO to Sn_3O_4 proceeds with decreasing pH, and the XRD patterns indicate the coexistence of SnO and Sn_3O_4 at pH 5 (Fig. 1(b)). Only Sn_3O_4 diffraction peaks were found to exist below pH 3, as shown in Figs. 1(d) and 1(e), where the ■ symbol was assigned to (111), ($\bar{2}$10), ($\bar{1}$21), and (311) of triclinic Sn_3O_4 (JCPDS-20-1293) [21]. Notably, several unknown crystalline peaks were observed as the pH approached 1. Thus, keeping the pH value between 2 and 3 during the reaction was critical for synthesizing well-defined Sn_3O_4 nanostructures.

Raman spectroscopy measurements also confirmed the phase transformation from SnO to Sn_3O_4 at pH 5. The Raman peaks were collected using a 514 nm excitation laser. Peaks at 113 and 211 cm^{-1} indicated the presence of SnO, as shown in Fig. 2(a). Peaks from the SnO and Sn_3O_4 structures coexisted at pH 5, as also observed from the XRD data (Fig. 1). As the pH was decreased, peaks corresponding to Sn_3O_4, at 143 and 170 cm^{-1}, gradually appeared, as shown in Fig. 2(b). At pH less than 3, only peaks corresponding to

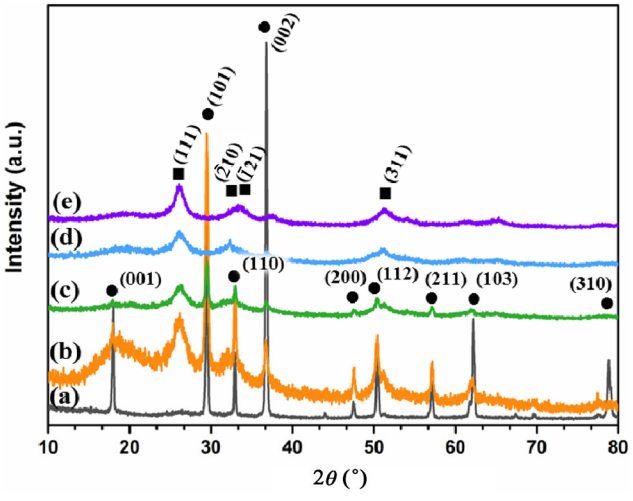

Figure 1 XRD patterns of the precipitates synthesized at different pH values; (a) SnO, (b) pH = 5, (c) pH = 4, (d) pH = 3, and (e) pH = 2 (●: SnO, ■: Sn_3O_4).

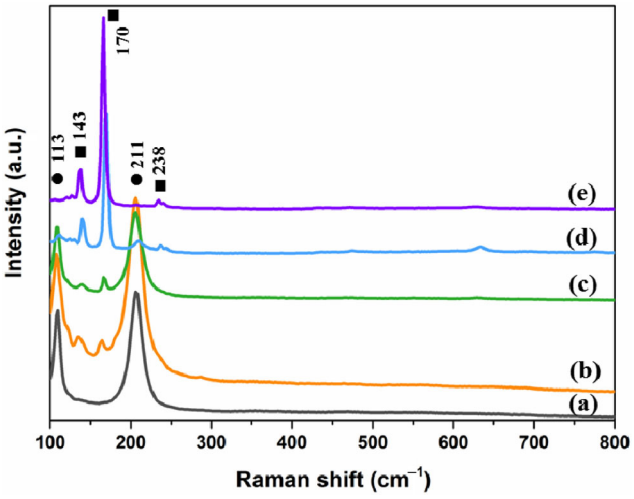

Figure 2 Raman spectra of the precipitates synthesized at different pH values; (a) SnO, (b) pH = 5, (c) pH = 4, (d) pH = 3, and (e) pH = 2 (●: SnO, ■: Sn_3O_4).

Sn_3O_4 were seen (Figs. 2(d)–2(e)), and these became more prominent with decreasing pH [17]. No other impurities were detected. Hence, XRD analyses and Raman spectra indicated the transition of the tin oxide crystal structure from tetragonal SnO to triclinic Sn_3O_4 at pH 5, and the sole existence of Sn_3O_4 between pH 2 and 3.

The morphology of Sn_3O_4 was observed by using SEM and TEM. Figure 3 shows the variation of hierarchical Sn_3O_4 morphology under different pH conditions. It was observed that pH had a great influence on the morphology of Sn_3O_4. Indeed, in the absence of HCl, only SnO nanoparticles aggregated together [31], as shown in Fig. 3(a). At pH 5, neighboring nanoparticles aggregated into prickly spheres with a diameter of approximately 100 nm (Fig. 3(b)). As the acidity of solution was increased (pH = 4, Fig. 3(c)), the prickly surface became more prominent. Below pH 3, the SnO was completely transformed into hierarchical Sn_3O_4, and the prickles dissolved and recrystallized into nanoplates, as shown in Figs. 3(d) and 3(e) [31]. Figure 3(f) shows a magnified hierarchical Sn_3O_4 nanosphere, having irregularly oriented thin nanoplates with a radius of 20 nm.

The TEM images in Figs. 4(a) and 4(b) clearly show the aggregated Sn_3O_4 nanospheres covered with the protruded thin nanoplates. Figures 4(c)–4(e) show the HRTEM images of a nanoplate at different pHs. During dissolution and recrystallization of the nanoplate, the

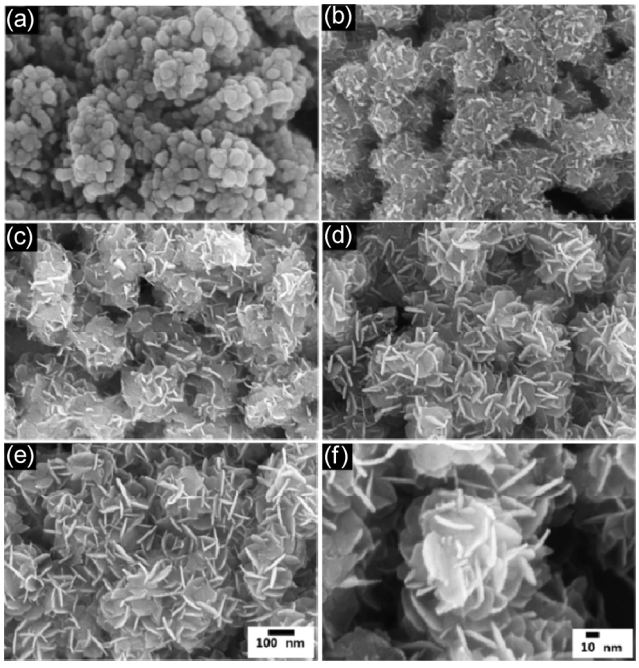

Figure 3 SEM images of the precipitates synthesized at different pH values; (a) SnO, (b) pH = 5, (c) pH = 4, (d) pH = 3, (e) pH = 2, and (f) a magnified SEM image of the hierarchical Sn_3O_4 nanospheres covered with nanoplates.

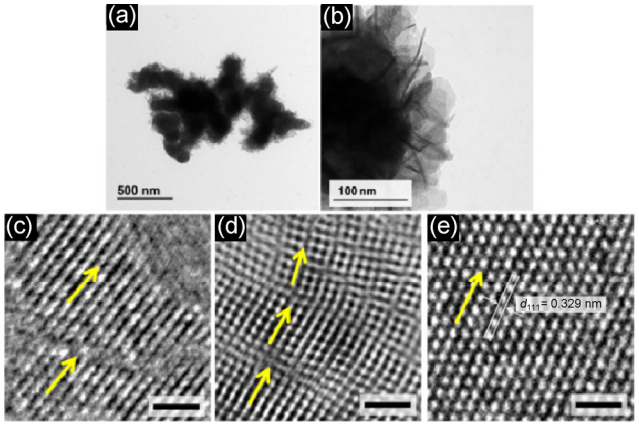

Figure 4 (a) TEM and (b) HRTEM image of the hierarchical Sn_3O_4 nanospheres covered with nanoplates. HRTEM images of nanoplates synthesized at (c) pH = 5, (d) pH = 4, and (e) pH = 2, showing the alignment of lattice fringes with decreasing pH (scale bar is 2 nm).

lattice was aligned along the direction of the more thermodynamically stable plane [32]. At pH 5, the nanoplate had conspicuous grain boundaries with an average grain size of 5 nm, and the lattice was misaligned between the grains (Fig. 4(c)). At pH 2, the grain boundaries disappeared and the lattice fringes became perfectly aligned along the [111] direction with

a spacing of 0.329 nm. Eventually, a single-crystalline triclinic phase corresponding to Sn_3O_4 nanoplates was formed under strongly acidic ambient conditions. However, the mechanisms of lattice alignment and nanoplate formation are not clearly understood.

3.2 Characterization of the hierarchical Sn_3O_4 nanostructure

The porous nature of the hierarchical Sn_3O_4 nanostructure was investigated by nitrogen (N_2) gas adsorption/desorption isotherm analyses, using the Brunauer-Emmett-Teller (BET) method, as shown in Fig. 5. All the hierarchical Sn_3O_4 nanostructures followed mesoporous type (IV) isotherm with a hysteresis loop. In the case of highly mesoporous materials, a hysteresis loop is observed due to the phenomenon of capillary condensation [33]. The BET surface area of SnO was found to be 8.92 $m^2 \cdot g^{-1}$. The other hierarchical Sn_3O_4 nanostructures, synthesized at different pH values, displayed BET surface areas of 11.68, 12.26, 46.48 and 55.05 $m^2 \cdot g^{-1}$ with decreasing pH values from 5 to 2, respectively. The amount of adsorbed nitrogen increased dramatically after complete conversion of SnO into the hierarchical Sn_3O_4. The Sn_3O_4 structure synthesized at pH 2 had the highest value of BET surface area, indicating a highly porous structure, resulting from intensive etching in such a strongly acidic ambient condition. The inset in Fig. 5 demonstrates the pore size distribution of hierarchical Sn_3O_4 synthesized at pH 2, revealing a maximum at 40 Å.

UV-visible absorption spectra of the Sn_3O_4 structures are shown in Fig. 6. In the case of SnO, no absorption was seen in the UV wavelengths and the absorption in the visible wavelengths was found to be negligible. The respective absorption edges corresponding to the Sn_3O_4 structures were observed at 397, 445, 480, and 550 nm, with decreasing pH values from 5 to 2, respectively. By using the equation of $E_g = 1240/\lambda$ (where λ is the absorption edge wavelength), the corresponding band gap of the Sn_3O_4 structures were calculated to be 3.12, 2.78, 2.58 and 2.25 eV, respectively. These results indicate that the band gap of hierarchical Sn_3O_4 nanostructure decreases with decreasing pH. In contrast to this, the commercially available P25 (TiO_2, Degusa) photocatalyst had an absorption edge of 350 nm, corresponding to a band gap of 3.54 eV, and a negligible absorbance at visible wavelengths.

The inset image in Fig. 6 shows that the color of the Sn_3O_4 structures varies from black to yellow, which corresponds to the powder of SnO and the hierarchical Sn_3O_4 structures synthesized with decreasing pH values. The observed UV-visible absorption spectra and the calculated band gap indicates that the hierarchical Sn_3O_4 nanostructure, synthesized in strongly acidic ambient conditions, can absorb both UV and

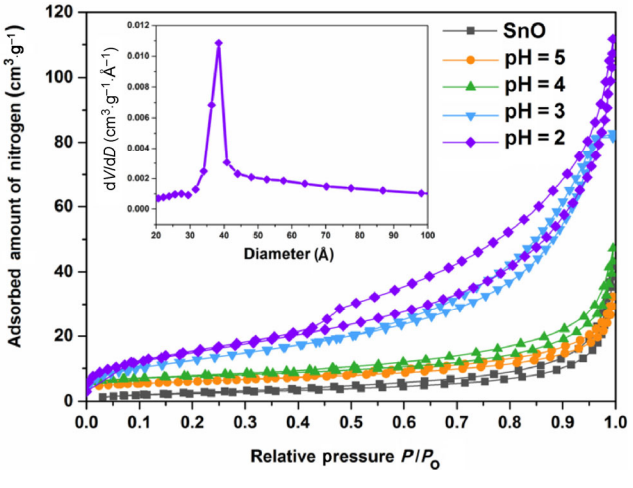

Figure 5 N_2 adsorption-desorption isotherms of all products. Inset figure is the pore-size distribution of the hierarchical Sn_3O_4 nanostructure synthesized at pH = 2.

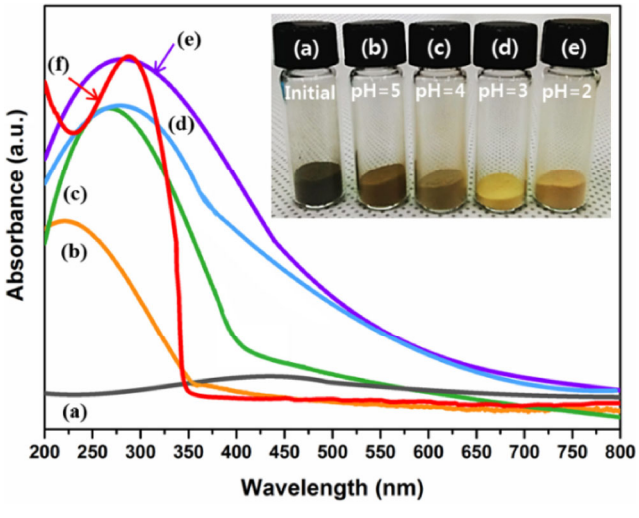

Figure 6 UV-Visible absorption spectra of the tin-related products; (a) SnO, (b) pH = 5, (c) pH = 4, (d) pH = 3, (e) pH = 2 and (f) P25. Inset image shows the color change of as-made powder synthesized at different pH values.

visible light. Thus, this material can effectively use the sunlight, from which most radiation comes in visible wavelengths with a spectrum peak at yellow wavelength.

3.3 Photocatalytic activity of the hierarchical Sn_3O_4 nanostructure

The photocatalytic activity of the mesoporous hierarchical Sn_3O_4 nanostructure synthesized at pH 2 was tested by measuring the photo-decomposition of MO under one sun condition (air mass 1.5). The P25 photocatalyst was also tested to compare its performance with the synthesized SnO and Sn_3O_4 structures. Since the P25 (TiO_2) photocatalyst has the merits of inexhaustible abundance with no photo-corrosion and non-toxicity [34–36], many research groups have studied its photocatalytic phenomena under irradiation with UV light [37–40]. However, due to its wide band gap, TiO_2 cannot excite electrons at the valence band under irradiation with visible light as shown in Fig. 6.

For direct comparison, the same amount of each photocatalyst (0.05 g) was added into an excessively concentrated (30 vol.%) MO solution in 100 mL DI water, respectively, to measure the photocatalytic ability in such an extreme condition (Fig. 7, discussed later). Usually, MO has been used as a pH indicator as well as in various industrial fields such as textile, printing, paper, food, etc. However, it has mutagenic side-effects and often pollutes the environment. Thus, the elimination of MO in solution is necessary for the environment and for promoting healthy life. When the photocatalyst absorbs light from the sun or an artificial light source, it produces electron-hole pairs. The generated holes attack the surrounding water molecules to generate hydroxyl radicals (*OH) at the surface of photocatalysts, as depicted in the following photo-oxidation reactions [41]

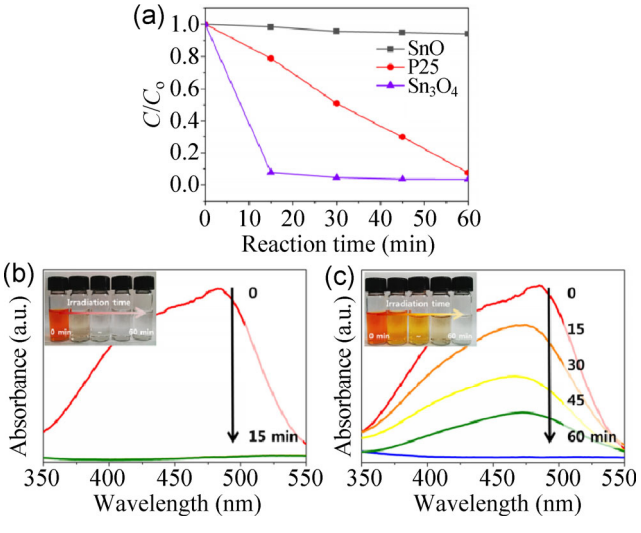

Figure 7 (a) A comparison of the photocatalytic activity of three different photocatalysts by measuring the photo-decomposition of MO solution under one sun condition. UV-visible absorption spectra of 0.05 g of (b) Sn_3O_4 and (c) P25 photocatalyst in MO solution, with varying irradiation time. The inset images show the color change of MO solution as a function of irradiation time.

$$\text{Metal oxide} + h\nu \rightarrow e^-_{CB} + h^+_{VB} \quad (1)$$

$$h^+_{VB} + H_2O \rightarrow {}^*OH + H^+ \quad (2)$$

It is known that the hydroxyl radical has the second largest oxidation potential of 2.8 V among several common oxidants including fluorine (3.03 V), ozone (2.07 V), hydrogen peroxide (1.77 V) and chloride (1.36 V). Therefore, the *OH radical can rapidly attack and cleave the aromatic rings of organic pollutants [42].

Figure 7(a) represents the variation of MO concentration (C/C_o) as a function of exposure time under one sun condition. The decomposition efficiency of the photocatalyst is defined as follows

$$\text{Photo-decomposition (\%)} = (1 - C/C_o) \times 100\ \% \quad (3)$$

where, C_o is the initial concentration of MO solution before irradiation and C is its concentration after irradiation. After 1 h exposure, no decomposition of MO was observed in the case of SnO, as it displayed a small BET surface area and a negligible light absorbance in the entire UV-Visible wavelength range. In the case of P25, the photo-decomposition proceeded slowly: 80% of the MO remained after 15 min exposure and it required 1 h to decompose all the MO contents, because this photocatalyst is active only at UV wavelengths. Unlike P25, the mesoporous hierarchical Sn_3O_4 nanostructure synthesized at pH 2 demonstrated a rapid photo-decomposition owing to its narrow band gap, enabling it to absorb the intense visible and UV light concurrently. Hence, the MO was completely decomposed within 15 min with only 0.05 g of Sn_3O_4 photocatalyst. Comparison of photocatalytic activity of P25 vs. Sn_3O_4 under UV light or visible light

illumination is illustrated in Fig. S1 of the Electronic Supplementary Material (ESM). The Sn_3O_4 showed a much higher photocatalytic activity in both cases.

Figures 7(b) and 7(c) present the variation of the absorption spectra of MO solution with different exposure times when using the Sn_3O_4 and P25, respectively. In the case of Sn_3O_4 photocatalyst, the intensity of the MO absorption peak (λ = 485 nm) was dramatically attenuated (Fig. 7(a)). After 15 min exposure, the color of the MO solution was bleached (as shown in the inset of Fig. 7(b)), suggesting that MO was completely decomposed within 15 min. In contrast, the MO absorption peak gradually decreased with exposure time, when using P25. The inset in Fig. 7(c) confirms the gradual color change of the solution with exposure time.

The photo-decomposition rate of MO can be calculated by the following equation [14]

$$-\ln(C/C_o) = \kappa t \quad (4)$$

where κ (min^{-1}) is the photo-decomposition rate constant. The κ value of each photocatalyst after 15 min irradiation is summarized in Table 1. The Sn_3O_4 exhibited much faster photo-decomposition activity compared with the other two photocatalysts. The κ value of Sn_3O_4 was calculated to be 1.73×10^{-1} min^{-1} under one sun condition, which is a 90.86% enhancement compared to that of P25 (1.58×10^{-2} min^{-1}). Considering the complete removal of the extremely concentrated MO solution (30 vol.%), the hierarchical Sn_3O_4 nanostructure shows excellent photocatalytic ability. This enhanced performance may be ascribed to its large surface area, permitting widespread contact with the MO solution, and its narrow band gap, which effectively utilizes the visible light of the Sun.

The used Sn_3O_4 photocatalysts were collected by centrifugation and recycled in the subsequent photocatalytic activity test to check the durability for repeatable use. No significant change in photocatalytic activity was observable in 5 successive tests (Fig. S2 in the ESM).

Table 1 Photo-decomposition rate of MO solution

Photocatalyst	Decompositon rate (κ, min^{-1})
(a) SnO	1.09×10^{-3}
(b) P25	1.58×10^{-2}
(c) Sn_3O_4	1.73×10^{-1}

4 Conclusion

Hierarchical Sn_3O_4 nanospheres covered with nanoplates were synthesized via a simple hydrothermal method in strongly acidic ambient conditions. X-ray diffraction and Raman spectroscopy evidenced that only triclinic Sn_3O_4 was produced from SnO at pH 3 by dissolution and recrystallization. During recrystallization, the lattice of the nanoplate was aligned along the thermodynamically stable [111] plane. The hierarchical Sn_3O_4 nanostructure (0.05 g) possessed an ability to fully decompose 30 vol.% MO in 100 mL DI solution in 15 min, under one sun condition, with a decomposition rate of 1.73×10^{-1} min^{-1}. This indicates a 90.86% enhancement, in the photocatalytic ability, compared with that of the commercially available P25. The high photo-decomposition activity of the hierarchical Sn_3O_4 nanostructure was suggested to be resulting from a high BET surface area of 55.05 $m^2 \cdot g^{-1}$ and a narrow band gap of 2.25 eV, which is capable of absorbing the visible light.

Acknowledgements

This work was supported by the Basic Science Research program through the National Research Foundation of Korea funded by the Pioneer Research Center Program (NRF, No. 2014M3C1A3016468) and the GIST Specialized Research Project provided by GIST.

Electronic Supplementary Material: Supplementary material (experimental details and additional data) is available in the online version of this article at http://dx.doi.org/10.1007/s12274-015-0855-2.

References

[1] Dai, Z. R.; Gole, J. L.; Stout, J. D.; Wang, Z. L. Tin oxide nanowires, nanoribbons, and nanotubes. *J. Phys. Chem. B* **2002**, *106*, 1274–1279.

[2] Pan, Z. W.; Dai, Z. R.; Wang, Z. L. Nanobelts of semiconducting oxides. *Science* **2001**, *291*, 1947–1949.

[3] Xu, X. X.; Zhuang, J.; Wang, X. SnO_2 quantum dots and quantum wires: Controllable synthesis, self-assembled 2D architectures, and gas-sensing properties. *J. Am. Chem. Soc.* **2008**, *130*, 12527–12535.

[4] Cheng, Y.; Chen, K. S.; Meyer, N. L.; Yuan, J.; Hirst, L. S.; Chase, P. B.; Xiong, P. Functionalized SnO_2 nanobelt field-effect transistor sensors for label-free detection of cardiac troponin. *Biosens. Bioelectron.* **2011**, *26*, 4538–4544.

[5] Ding, S. J.; Chen, J. S.; Qi, G. G.; Duan, X. N.; Wang, Z. Y.; Giannelis, E. P.; Archer, L. A.; Lou, X. W. Formation of SnO_2 hollow nanospheres inside mesoporous silica. *J. Am. Chem. Soc.* **2011**, *133*, 21–23.

[6] Song, H.; Lee, K.-H.; Jeong, H.; Um, S. H.; Han, G.-S.; Jung, H. S.; Jung, G. Y. A simple self-assembly route to single crystalline SnO_2 nanorod growth by oriented attachment for dye sensitized solar cells. *Nanoscale* **2013**, *5*, 1188–1194.

[7] Shi, L. A.; Lin, H. L. Facile fabrication and optical property of hollow SnO_2 spheres and their application in water treatment. *Langmuir* **2010**, *26*, 18718–18722.

[8] Wang, H. J.; Sun, F. Q.; Zhang, Y.; Li, L. S.; Chen, H. Y.; Wu, Q. S.; Yu. J. C. Photochemical growth of nanoporous SnO_2 at the air-water interface and its high photocatalytic activity. *J. Mater. Chem.* **2010**, *20*, 5641–5645.

[9] Nasr, C.; Kamat, P. V.; Hotchandani, S. Photoelectrochemical behavior of coupled SnO_2/CdSe nanocrystalline semiconductor films. *J. Electroanal. Chem.* **1997**, *420*, 201–207.

[10] Kar, A.; Kundu, S.; Patra, A. Photocatalytic properties of semiconductor SnO_2/CdS heterostructure nanocrystals. *RSC Adv.* **2012**, *2*, 10222–10230.

[11] Vlachopoulos, N.; Liska, P.; Augustynski, J.; Gratzel, M. Very efficient visible light energy harvesting and conversion by spectral sensitization of high surface area polycrystalline titanium dioxide films. *J. Am. Chem. Soc.* **1988**, *110*, 1216–1220.

[12] Wrighton, M. S.; Ginley, D. S.; Wolczanski, P. T.; Ellis, A. B.; Morse, D. L.; Linz, A. Photoassisted electrolysis of water by irradiation of a titanium dioxide electrode. *Proc. Natl. Acad. Sci. USA.* **1975**, *72*, 1518–1522.

[13] He, Y. H.; Li, D. Z.; Chen, J.; Shao, Y.; Xian, J. J.; Zheng, X. Z.; Wang, P. Sn_3O_4: A novel heterovalent-tin photocatalyst with hierarchical 3D nanostructures under visible light. *RSC Adv.* **2014**, *4*, 1266–1269.

[14] Xia, W. W.; Wang, H. B.; Zeng, X. H.; Han, J.; Zhu, J.; Zhou, M.; Wu, S. D. High-efficiency photocatalytic activity of type II SnO/Sn_3O_4 heterostructures via interfacial charge transfer. *CrystEngComm* **2014**, *16*, 6841–6847.

[15] Berengue, O. M.; Simon, R. A.; Chiquito, A. J.; Dalmaschio, C. J.; Leite, E. R.; Guerreiro, H. A.; Guimarães, F. E. G. Semiconducting Sn_3O_4 nanobelts: Growth and electronic structure. *J. Appl. Phys.* **2010**, *107*, 033717.

[16] Lawson, F. Tin oxide-Sn_3O_4. *Nature* **1967**, *215*, 955–956.

[17] Wang, F. P.; Zhou, X. T.; Zhou, J. G.; Sham, T. K.; Ding, Z. F. Observation of single tin dioxide nanoribbons by confocal raman microspectroscopy. *J. Phys. Chem. C* **2007**, *111*, 18839–18843.

[18] Seko, A.; Togo, A.; Oba, F.; Tanaka, I. Structure and stability of a homologous series of tin oxides. *Phys. Rev. Lett.* **2008**, *100*, 045702.

[19] Mäki-Jaskari, M. A.; Rantala, T. T. Possible structures of non-stoichiometric tin oxide: The composition Sn_2O_3. *Modell. Simul. Mater. Sci. Eng.* **2004**, *12*, 33–41.

[20] White, T. A.; Moreno, M. S.; Midgley, P. A. Structure determination of the intermediate tin oxide Sn_3O_4 by precession electron diffraction. *Z. Kristallogr.* **2010**, *225*, 56–66.

[21] Gauzzi, F.; Verdini, B.; Maddalena, A.; Principi, G. X-ray diffraction and mössbauer analyses of SnO disproportionation products. *Inorg. Chim. Acta* **1985**, *104*, 1–7.

[22] Moreno, M. S.; Mercader, R. C.; Bibiloni, A. G. Study of intermediate oxides in SnO thermal decomposition. *J. Phys.: Condens. Mat.* **1992**, *4*, 351–355.

[23] Damaschio, C. J.; Berengue, O. M.; Stroppa, D. G.; Simon, R. A.; Ramirez, A. J.; Schreiner, W. H.; Chiquito, A. J.; Leite, E. R. Sn_3O_4 single crystal nanobelts grown by carbothermal reduction process. *J. Cryst. Growth* **2010**, *312*, 2881–2886.

[24] Cahen, S.; David, N.; Fiorani, J. M.; Maître, A.; Vilasi, M. Thermodynamic modelling of the O-Sn system. *Thermochimica Acta* **2003**, *403*, 275–285.

[25] Ohgi, H.; Maeda, T.; Hosono, E.; Fujihara, S.; Imai, H. Evolution of nanoscale SnO_2 grains, flakes, and plates into versatile particles and films through crystal growth in aqueous solutions. *Cryst. Growth Des.* **2005**, *5*, 1079–1083.

[26] Uchiyama, H.; Ohgi, H.; Imai, H. Selective preparation of SnO_2 and SnO crystals with controlled morphologies in an aqueous solution system. *Cryst. Growth Des.* **2006**, *6*, 2186–2190.

[27] Manikandan, M.; Tanbe, T.; Li, P.; Ueda, S.; Ramesh, G. V.; Kodiyath, R.; Wang, J. J.; Hara, T.; Dakshanamoorthy, A.; Ishihara, S. et al. Photocatalytic water splitting under visible light by mixed-valence Sn_3O_4. *ACS Appl. Mater. Interfaces* **2014**, *6*, 3790–3793.

[28] Xu, W.; Li, M.; Chen, X. B.; Zhao, J. H.; Tan, R. Q.; Li, R.; Li, J.; Song, W. J. Synthesis of hierarchical Sn_3O_4 microflowers self-assembled by nanosheets. *Mater. Lett.* **2014**, *120*, 140–142.

[29] Li, M.; Tan, R. Q.; Li, R.; Song, W. J.; Xu, W. Effects of pH on the microstructures and optical properties of Sn_3O_4 crystals prepared by hydrothermal method. *Ceram. Int.* **2014**, *40*, 11381–11385.

[30] Davies, C. G.; Donaldson, J. D. The mössbauer effect in tin(II) compounds, Part III. The spectra of trihydroxostannates(II)

and of basic tin(II) salts. *J. Chem. Soc. A* **1968**, 946–948.

[31] Bavykin, D. V.; Friedrich, J. M.; Walsh, F. C. Protonated titanates and TiO_2 nanostructured materials: Synthesis, properties, and applications. *Adv. Mater.* **2006**, *18*, 2807–2824.

[32] Wu, J. M.; Hayakawa, S.; Tsuru, K.; Osaka, A. Porous titania films prepared from interactions of titanium with hydrogen peroxide solution. *Scr. Mater.* **2002**, *46*, 101–106.

[33] Sing, K. S. W.; Everett, D. H.; Haul, R. A. W.; Moscou, L.; Pierotti, R. A.; Rouquérol, J.; Siemieniewska, T. Physical and biophysical chemistry division commission on colloid and surface chemistry including catalysis. *Pure Appl. Chem.* **1985**, *57*, 603–619.

[34] Ding, Y. H.; Zhang, P.; Long, Z. L.; Jiang, Y.; Xu, F.; Lei, J. G. Fabrication and photocatalytic property of TiO_2 nanofibers. *J. Sol-Gel Sci. Technol.* 2008, *46*, 176–179.

[35] Bocarsly, A. B.; Bolts, J. M.; Cummins, P. G.; Wrighton, M. S. Photoelectrolysis of water at high current density: Use of ultraviolet laser excitation. *Appl. Phys. Lett.* **1977**, *31*, 568–570.

[36] Sclafani, A.; Mozzanega, M.-N.; Pichat, P. Effect of silver deposits on the photocatalytic activity of titanium dioxide samples for the dehydrogenation or oxidation of 2-propanol. *J. Photochem. Photobiol. A: Chem.* **1991**, *59*, 181–189.

[37] Doodeve, C. F.; Kitchener, J. A. The mechanism of photosensitisation by solids. *Trans. Faraday Soc.* **1938**, *34*, 902–908.

[38] Fox, M. A.; Dulay, M. T. Heterogeneous photocatalysis. *Chem. Rev.* **1993**, *93*, 341–357.

[39] Wang, R.; Hashimoto, K.; Fujishima, A.; Chikuni, M.; Kojima, E.; Kitamura, A.; Shimohigoshi, M.; Watanabe, T. Light-induced amphiphilic surface. *Nature* **1997**, *388*, 431–432.

[40] Han, C.; Wang, Y. D.; Lei, Y. P.; Wang, B.; Wu, N.; Shi, Q.; Li, Q. *In situ* synthesis of graphitic-C_3N_4 nanosheet hybridized N-doped TiO_2 nanofibers for efficient photocatalytic H_2 production and degradation. *Nano Res.* **2015**, *8*, 1199–1209.

[41] Fujishima, A.; Honda, K. Electrochemical photolysis of water at a semiconductor electrode. *Nature* **1972**, *238*, 37–38.

[42] Hoigné, J.; Bader, H. The role of hydroxyl radical reactions in ozonation processes in aqueous solutions. *Water Res.* **1976**, *10*, 377–386.